



A Framework for Three-Dimensional Mesoscale Modeling of Anisotropic Swelling and Mechanical Deformation in Lithium-Ion Electrodes

Scott A. Roberts,^{*,z} Victor E. Brunini, Kevin N. Long, and Anne M. Grillet*

Sandia National Laboratories, Albuquerque, New Mexico 87185-0836, USA

Lithium-ion battery electrodes rely on a percolated network of solid particles and binder that must maintain a high electronic conductivity in order to function. Coupled mechanical and electrochemical simulations may be able to elucidate the mechanisms for capacity fade. We present a framework for coupled simulations of electrode mechanics that includes swelling, deformation, and stress generation driven by lithium intercalation. These simulations are performed at the mesoscale, which requires 3D reconstruction of the electrode microstructure from experimental imaging or particle size distributions. We present a novel approach for utilizing these complex reconstructions within a finite element code. A mechanical model that involves anisotropic swelling in response to lithium intercalation drives the deformation. Stresses arise from small-scale particle features and lithium concentration gradients. However, we demonstrate, for the first time, that the largest stresses arise from particle-to-particle contacts, making it important to accurately represent the electrode microstructure on the multi-particle scale. Including anisotropy in the swelling mechanics adds considerably more complexity to the stresses and can significantly enhance peak particle stresses. Shear forces arise at contacts due to the misorientation of the lattice structure. These simulations will be used to study mechanical degradation of the electrode structure through charge/discharge cycles.

© The Author(s) 2014. Published by ECS. This is an open access article distributed under the terms of the Creative Commons Attribution Non-Commercial No Derivatives 4.0 License (CC BY-NC-ND, <http://creativecommons.org/licenses/by-nc-nd/4.0/>), which permits non-commercial reuse, distribution, and reproduction in any medium, provided the original work is not changed in any way and is properly cited. For permission for commercial reuse, please email: oa@electrochem.org. [DOI: 10.1149/2.0081411jes] All rights reserved.

Manuscript received June 23, 2014. Published September 5, 2014. This was Paper 318 presented at the Orlando, Florida, Meeting of the Society, May 11–15, 2014. *This paper is part of the JES Focus Issue on Mechano-Electro-Chemical Coupling in Energy Related Materials and Devices.*

Capacity fade in lithium-ion batteries (LIB) is potentially influenced by a large number of mechanisms,¹ one of which is mechanical degradation of the electrode microstructure. Both electrodes experience mechanical deformation, and in this paper, we focus on the cathode of the lithium-cobalt-oxide (LiCoO₂, or LCO) system.² Cathodes are made up of a three-dimensional (3D), percolating, bicontinuous network consisting of solid, electroactive particles, a polymer binder, and electrolyte. The bicontinuous nature of this network is critical, as Li⁺ ions must be able to transport from the anode, through the separator, to any particle in the cathode via the electrolyte. At the same time, electrons must be able to transport through the solid particle network to the current collector. Any particle that becomes physically isolated from, or poorly connected to, its network or from the electrolyte does not contribute to the electrochemical reactions, resulting in capacity loss.

One way in which particles may become disconnected from their network is by the swelling, shrinking, and fracture mechanisms that may occur through many charge-discharge cycles.³⁻⁶ As lithium intercalates into the electrode particles, the crystal lattice spacing may change either isotropically or anisotropically. For LiCoO₂ cathodes in particular, the crystal lattice shrinks anisotropically upon lithium intercalation.^{7,8} As was measured by Reimers and Dahn,⁷ and later in more detail by Amatucci et al.,⁸ the lattice shrinkage upon lithiation can be quite significant and is anisotropic in nature. Cannarella and Arnold⁹ also showed how external stresses affect battery life in pouch cells. This shrinkage, and the resulting swelling as lithium leaves the lattice, can cause great mechanical stresses, particularly when the particles are physically constrained, as they are in a cathode. These stresses may lead to the particle fracturing, with smaller pieces separating from the network, or slipping at particle-particle boundaries, also possibly leading to particle disconnection. Alternatively, the swelling and shrinking phenomena may simply change the particle contact area, and therefore the effective internal or contact resistances. There-

fore, understanding how and where stresses are formed on lithiation is important to better understanding capacity fade in LIB.

Reconstruction of realistic microstructures using focused ion beam scanning electron microscope (FIB/SEM) techniques has been an area of much recent interest. LIB cathode reconstructions have been used to investigate intrinsic features of the microstructure, such as porosity and tortuosity,¹⁰⁻¹⁵ focusing on the solid particles only. Later, researchers differentiated between particle, binder, and electrolyte,^{16,17} getting a better grasp of the effective material properties.

More recent studies have used these reconstructed geometries to perform detailed species transport and electrochemical simulations, typically in a finite volume framework.¹⁸⁻²⁰ Wiedemann et al.¹⁹ clearly demonstrated how the complex shape of reconstructed particles changed the electrochemical behavior over more simplistic spherical representations. The effect of anisotropic diffusion of lithium through the particle has also been studied.²¹⁻²³

Efforts to understand the mechanics of real electrodes, however, have primarily focused on single, isolated particles due to the difficulty in creating a mesh appropriate for finite element simulations. Multiple groups have demonstrated that lithiation-induced stresses strongly depend on the geometry, with maximum stresses being much greater in realistic single particle shapes than in spherical particles.^{3,21,25} These studies all assumed that the particles were isolated and isotropic. Park et al.⁴ included the effect of phase-transformation-induced stresses in their simulations, finding the phase transformation effect to be significant. Malave et al.²⁶ performed a similar analysis, but included the effect of anisotropic swelling with phase change, using the experimental data of Reimers and Dahn⁷. Still others have looked at particle fracture.⁵ On a larger length scale, Awarke et al.²⁴ used representative volume elements to understand how strains and external loads affected particle properties using a spherical particle pack. Very recently, Chung et al.²⁷ used 3D reconstructions from X-ray tomography of LiMn₂O₄ to study the effect of particle size polydispersity and surface roughness on battery performance. While simple mechanics were included in this work, their focus was not on understanding how the electrode structure evolves, potentially driving capacity fade.

*Electrochemical Society Active Member.

^zE-mail: sarober@sandia.gov

Even with all of this attention in the literature, few, if any, studies have investigated how the network configuration and microstructure affects electrode mechanics and performance. In this paper, we develop a framework for finite element method (FEM) simulations of the anisotropic swelling and stress generation in a LIB cathode percolating network. We also report on the development of confinement stresses due to the particle microstructure. We perform these simulations on representative microstructures obtained from particle size distributions and experimental studies using FIB/SEM techniques, deploying a novel computational method to ease the burden of mesh creation. In the “Model” section, the governing equations for modeling the electrochemistry and mechanics are described. Procedures for constructing relevant microstructures are presented in the “Geometric Representation” section, and the details of the numerical methods are shown in the “Numerical Methods” section. Two sets of demonstration simulations are shown in the “Demonstration Problems” section, and we present some concluding thoughts and ideas for future study in the “Conclusions” section.

Model

In this section, we present the governing equations used to solve for the species concentration and the mechanical deformation and stresses in a LiCoO₂ cathode. A simplified schematic of the geometry we consider is shown in Figure 1. For simplicity, we show only three particles, each shown in a different shade of green. Because the particles are separated, each particle has a different orientation of its crystal lattice, shown by the local \mathbf{n}/t coordinate systems in the figure. While in this 2D schematic the electrolyte regions do not appear to be continuous, in 3D it is a bicontinuous network of particles and electrolyte. Lithium ions are supplied to the cathode from the separator via the electrolyte, and electrons are removed via the current collector.

Electrochemistry.— The electrochemical model consists of distinct volumetric equations solved in the particle and electrolyte domains depicted in Figure 1, coupled by boundary conditions modeling the intercalation reaction at the particle-electrolyte interface. Our modeling approach builds on that of Wiedemann et al. by including the transport of Li⁺ and is similar to that of Hutzenlaub et al.^{19,20} Electron transport in the particles is modeled by applying current conservation to Ohm’s law,

$$\nabla \cdot (\kappa \nabla \phi_s) = 0, \quad [1]$$

and solving for the solid phase voltage, ϕ_s , where κ is the solid-phase electrical conductivity. Lithium transport within the particles is modeled by solving a species conservation equation with a Fickian

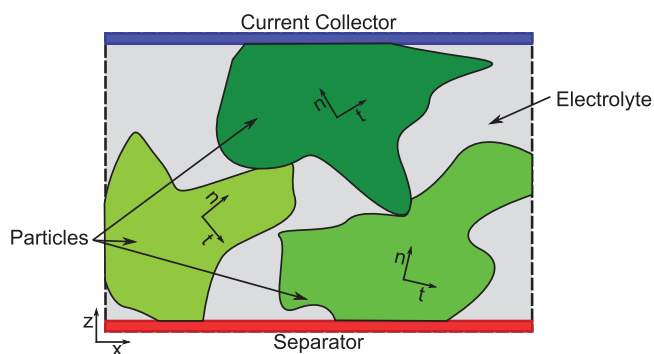


Figure 1. Small-scale schematic of the cathode configuration considered in this work. The separator is at the bottom of the domain (red) with a current collector located at top (blue). Three solid particles are shown in green, with each shade of green denoting a separate particle, surrounded by electrolyte (gray). Particles are typically on the length scale of 5-10 microns.

diffusion model,

$$\frac{\partial C_{\text{Li}}}{\partial t} + \nabla \cdot (-D_{\text{Li}} \nabla C_{\text{Li}}) = 0, \quad [2]$$

and solving for the concentration of Li, C_{Li} . Currently, we treat the diffusivity of lithium, D_{Li} , to be constant and isotropic. In future work we plan to include the contribution from the activity coefficient of Li to the flux of Li and utilize an anisotropic D_{Li} .

Similarly, in the electrolyte we apply current (3) and species (4) conservation to solve for the liquid phase voltage, ϕ_l , and lithium ion concentration, C_{Li^+} . The current conservation equation for the electrolyte includes contributions from both the Li⁺ cation and PF₆⁻ anion.

$$\nabla \cdot [F(\mathbf{J}_{\text{Li}^+} - \mathbf{J}_{\text{PF}_6^-})] = 0 \quad [3]$$

$$\frac{\partial C_{\text{Li}^+}}{\partial t} + \nabla \cdot \mathbf{J}_{\text{Li}^+} = 0 \quad [4]$$

The fluxes of both ions (Li⁺ and PF₆⁻) are calculated using a Nernst-Planck model,

$$\mathbf{J}_i = -D_i \left(z_i C_i \frac{F}{RT} \nabla \phi_l + \nabla C_i \right), \quad [5]$$

where z_i is the species valence, R is the gas constant, F is Faraday’s constant, and T is the absolute temperature. Finally, we assume electroneutrality to determine the anion concentration, $C_{\text{PF}_6^-} = C_{\text{Li}^+}$. We are not considering a stress-flux coupling, which could be present in battery materials, such as LiSi, that experience large volume changes on intercalation.

The volumetric equations in the particle and electrolyte domains are coupled by the boundary conditions modeling the intercalation reaction at the particle-electrolyte interface. The electrochemical reaction kinetics are modeled using the Butler-Volmer equation, (6). The equilibrium voltage for LCO (ϕ_{eq}) is modeled using the fit from Doyle and Fuentes.²⁸

$$r = j_0 \left[\exp \left(\frac{\alpha_a F (\phi_s - \phi_l - \phi_{\text{eq}})}{RT} \right) - \exp \left(\frac{-\alpha_c F (\phi_s - \phi_l - \phi_{\text{eq}})}{RT} \right) \right] \quad [6]$$

Here, j_0 is the exchange current density and the α_i are the charge transfer coefficients. The computed intercalation reaction rate, r , is used to apply normal flux boundary conditions to each of the volumetric conservation equations, as specified below:

$$-\kappa \nabla \phi_s \cdot \mathbf{n} = -r \quad [7]$$

$$-D_{\text{Li}} \nabla C_{\text{Li}} \cdot \mathbf{n} = \frac{r}{F} \quad [8]$$

$$F(\mathbf{J}_{\text{Li}^+} - \mathbf{J}_{\text{PF}_6^-}) \cdot \mathbf{n} = r \quad [9]$$

$$\mathbf{J}_{\text{Li}^+} \cdot \mathbf{n} = -\frac{r}{F} \quad [10]$$

In the context of this sub-section, \mathbf{n} is the normal vector pointing from the particle surface into the electrolyte. Particle-to-particle contacts are considered to be in perfect contact.

Finally, boundary conditions must be specified at the separator and current collector interfaces to fully define the model. At the separator boundary we apply Dirichlet conditions for the solid phase voltage ($\phi_s = 0$) and lithium ion concentration ($C_{\text{Li}^+} = C_{\text{Li}^+}^0$), and no-flux boundaries for the solid current ($-\kappa \nabla \phi_s \cdot \mathbf{n} = 0$) and Li conservation ($-D_{\text{Li}} \nabla C_{\text{Li}} \cdot \mathbf{n} = 0$) equations. At the current collector boundary we apply no-flux conditions to the electrolyte current conservation ($F(\mathbf{J}_{\text{Li}^+} - \mathbf{J}_{\text{PF}_6^-}) \cdot \mathbf{n} = 0$) and lithium ion conservation ($\mathbf{J}_{\text{Li}^+} \cdot \mathbf{n} = 0$) equations as well as the solid lithium conservation equation ($-D_{\text{Li}} \nabla C_{\text{Li}} \cdot \mathbf{n} = 0$). Finally, we apply either a Dirichlet condition for ϕ_s or a constant current condition ($-\kappa \nabla \phi_s \cdot \mathbf{n} = r$) to the solid phase current equation to model potentiostatic or galvanostatic conditions as desired.

Mechanics.— The balance of linear momentum in the solid structure is considered to be in quasi-static equilibrium, yielding the governing equation

$$\nabla \cdot \boldsymbol{\sigma} + \mathbf{b} = \mathbf{0}, \quad [11]$$

where $\boldsymbol{\sigma}$ is the Cauchy stress tensor and \mathbf{b} represents an applied body force density. We consider motion in the small deformation limit and model the constitutive response of the particles as linear with respect to the elastic strain portion of the total small strain tensor. Hence, the constitutive response is

$$\boldsymbol{\sigma} = \mathbb{C} : (\boldsymbol{\varepsilon} - \boldsymbol{\beta} \Delta C_{\text{Li}}), \quad [12]$$

where \mathbb{C} is the fourth-rank elasticity tensor, $\boldsymbol{\varepsilon}$ is the total small strain tensor, and $\boldsymbol{\beta} \Delta C_{\text{Li}}$ represents the swelling strains that develop due to lithium intercalation. The small strain tensor is defined as the symmetric part of the Lagrangian displacement gradient, $\nabla \mathbf{d}$,

$$\boldsymbol{\varepsilon} = \frac{1}{2} [\nabla \mathbf{d} + (\nabla \mathbf{d})^T]. \quad [13]$$

Lithium intercalation generates swelling strain in (11), but the stress response occurs only if the total strain is different from the swelling strain in (12), which can occur due to particle-particle interactions, non-uniform lithium concentrations, and/or other mechanical boundary conditions. This swelling strain is governed by the change in lithium concentration from the stress-free initial conditions, $\Delta C_{\text{Li}} = C_{\text{Li}} - C_{\text{Li}}^0$, and a second-rank tensor, $\boldsymbol{\beta}$, which is a material parameter defined such that $\boldsymbol{\beta} = \boldsymbol{\varepsilon} / \Delta C_{\text{Li}}$. This approach is analogous to Vegard's law,²⁹ which is often used for metal alloy compositions and thermal strains.

Swelling behavior due to lithium intercalation in LCO cathodes is anisotropic.⁸ Specifically, the strain of the lattice in the direction normal to the crystal plane is different from that tangential to the plane, a behavior represented by a transversely isotropic model,

$$\hat{\boldsymbol{\beta}} = \begin{bmatrix} \beta_n & 0 & 0 \\ 0 & \beta_t & 0 \\ 0 & 0 & \beta_t \end{bmatrix}. \quad [14]$$

Here, $\hat{\boldsymbol{\beta}}$ is $\boldsymbol{\beta}$, but located in the coordinate system defined by the crystal structure of the particle, with \mathbf{x} aligning with the normal vector of the lattice, $\hat{\mathbf{n}}$. As each particle may be arbitrarily oriented in the simulation, (14) must be rotated into the laboratory reference frame using $\boldsymbol{\beta} = \mathbf{R} \cdot \hat{\boldsymbol{\beta}} \cdot \mathbf{R}^T$, where \mathbf{R} is the appropriate rotation matrix for this transformation. For a material that behaves isotropically, $\beta_n = \beta_t$.

This model could easily be extended to larger deformations by replacing the small strain tensor $\boldsymbol{\varepsilon}$ with an appropriate finite strain measure, such as the Green-Lagrange tensor \mathbf{E} . Then, (12) would provide the second Piola-Kirchhoff stress tensor, \mathbf{S} , which could be pushed forward to the current configuration using the deformation gradient tensor \mathbf{F} , $\mathbf{S} = \det(\mathbf{F}) \mathbf{F}^{-1} \cdot \boldsymbol{\sigma} \cdot \mathbf{F}^{-T}$.

Geometric Representation

In order to perform simulations on battery microstructures, we must be able to represent their complex geometry within the computational code. In this section, we present two methods to generate this geometrical representation. First, we describe how to generate the 3D microstructure from a specified particle size distribution. Then, we use experimentally generated images to reconstruct the microstructure for a real cathode material.

Reconstruction from spherical particles.— A relatively straightforward method of generating a 3D microstructure is to directly create one using a spherical particle size distribution. Drying was modeled using a discrete element approach implemented in the LAMMPS³¹ software package. Particles were modeled as spheres with rotational and translational degrees of freedom, with diameters drawn randomly from the experimentally measured particle size distribution for a nickel, manganese, cobalt (NMC 111) cathode material (Figure 2).³⁰

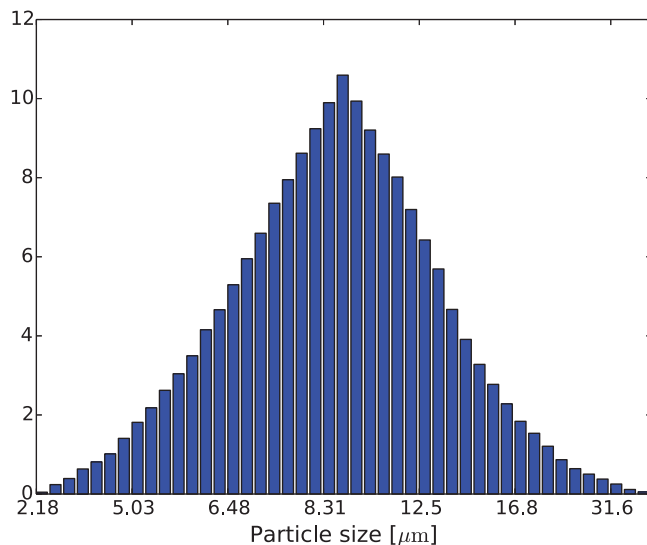


Figure 2. Particle size distribution used in creating the spherical particle reconstruction of §3.1.³⁰ The x -axis is a logarithmic distribution.

Starting configurations were constructed by randomly placing particles in a simulation domain of size $80 \times 80 \times 120$ microns to attain an initial volume fraction of approximately 0.25. For the data presented here, a relatively small system of 275 particles was used. The solvent was modeled using a recently developed technique known as Fast Lubrication Dynamics (FLD).^{32,33} For particles in contact, a Hertzian granular contact potential was used that includes normal and tangential contact and damping forces, as well as frictional yield.³⁴ Explicit integration of the equations of motion was carried out to simulate the evolution of particle positions.

The drying process was modeled by moving a flat surface at a prescribed velocity from the top of the simulation box downwards (in the $-z$ -direction). A granular contact wall was placed at the bottom boundary ($z = 0$), and periodic boundaries were maintained in the x and y directions. Buoyancy effects and volume fraction corrections to hydrodynamic drag in relation to the moving drying front were both included in the model; however, capillary interactions were not accounted for, due to difficulties in obtaining reliable approximations of capillary forces for crowded surfaces.³⁵

System parameters were set to match the experimental manufacturing process conditions as closely as possible, but several approximations were necessary due to computational constraints. For purposes of parametrizing the Hertzian granular contact potential, the Young's modulus was set to 10^3 Pa. This value is unrealistically low for cathode materials, but we do not expect it to have a qualitative impact on bulk granular dynamics or structure formation.³⁴ This approximation allows us to simulate the drying process over several seconds of real time, which is approaching relevant experimental time scales. Additionally, the solvent viscosity for the FLD model was set to 1.68 cP, corresponding to the viscosity of the *n*-methylpyrrolidone (NMP) solvent used in the manufacturing process, and densities of particles and solvent were set to realistic values (2.7 and 1.0 g/cm³, respectively). The binder was neglected. In all cases, the simulation was run until drying was complete (i.e. the drying front reached the bottom of the simulation domain), at which point particle motion ceased.

Once the particle packing is obtained from the drying solution, the particle radii and center locations are output to a text file. These are then read into Cubit³⁶ using a custom-built python script and used to generate spheres in Cubit. Since the drying simulation allows the particles to be deformable, recreating them in Cubit may cause particles to overlap. Where the particles overlap, they are joined, and then recut with the curve that joins the two particles. This effectively creates a plane that represents the interface between the two particles. The resulting geometry is shown in Figure 3.

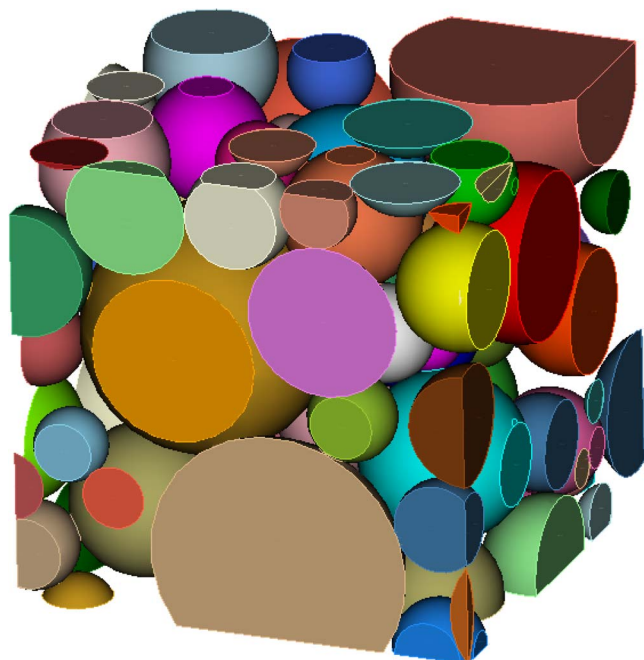


Figure 3. Three-dimensional reconstruction of a NMC 111 cathode from a particle size distribution, showing individual particles as different colors.

Once any overlaps are resolved, the particles are exported individually in the Standard Tessellation Language (STL) file format. Because each particle may have a different crystal lattice orientation and we wish to model their anisotropy, each particle is exported as a separate STL file. This enables them to be addressed individually within the simulation to assign different lattice orientations.

Reconstruction from experimental imaging.— Many recent studies^{19,26,27} have recognized that the exact surface shape of real electrode materials provide variations in performance that cannot be captured with idealized microstructures, such as collections of spheres. Therefore, we construct 3D microstructures that are based on experimental observations of an actual cathode electrode. We were kindly provided with a stack of 2D binarized images for a LiCoO₂ microstructure from a new VARTA LIC 18650 WC LIB by Hutzenlaub et al.,¹⁷ who obtained these images using FIB/SEM techniques. We refer the reader to Hutzenlaub et al.¹⁷ for details on obtaining and binarizing the 2D images.

The 2D images were compiled into a 3D voxel representation using the DREAM.3D software package.³⁷ This representation defines three phases, the LiCoO₂ particle phase, the polymer binder, and electrolyte/void. For this analysis, we only consider the effects of the particles, and the binder and electrolyte phases are merged and treated as all electrolyte for the purposes of lithium diffusion. This simplification will be resolved in future work. A surface mesh was created on the particle surface using the Multi-Material Marching Cubes algorithm.³⁷ This mesh was then smoothed with the Laplacian Smoothing Filter, and finally exported in the STL file format. The resulting faceted surface mesh is shown in Figure 4.

Because considering anisotropic stresses requires separate particle representations, we will later discuss the effect of isotropic confinement stresses generated during delithiation. Anisotropic stresses coupled with these realistic cathode structures will be addressed in a later publication.

Numerical Methods

The model described previously is solved using the Finite Element Method (FEM), implemented in Sierra/Multi-Mechanics Mod-

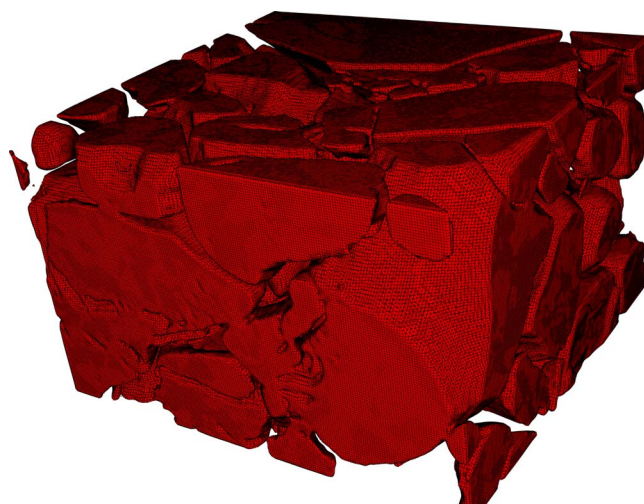


Figure 4. Three-dimensional reconstruction and surface mesh of a LiCoO₂ cathode.¹⁷

ule Aria.³⁸ The problem is solved on a tetrahedral element mesh using linear (Q1) basis functions. We consider these elements suitable for the solid mechanics representation since we are considering a compressible elastic response. The electrochemistry and mechanics equations are solved in separate equation systems, with each system using a Newton-Raphson nonlinear iteration scheme. While the physics are two-way coupled, the coupling from the mechanics to the electrochemistry is only through the Lagrangian deformation of the mesh. For these simulations, the deformations are quite small, making the coupling weak. This allows the segregated loose coupling scheme to work for this problem. The systems are evolved in time using a standard second-order backward differentiation formula (BDF2).

In order to solve the equations accurately on a complex domain such as that shown in Figure 4, a mesh that is conformal to the particle/electrolyte interface is required. However, manually creating this mesh in a mesh generation package such as Cubit³⁶ is not a trivial process, and may be intractable in reasonable time. Therefore, we employ the Conformal Decomposition Finite Element Method (CDFEM)³⁹ to create a computable, conformal mesh. This method generates a mesh which accurately captures the complex particle surfaces with mesh faces, while relying on a simply-generated background mesh for the particle interiors.

First, a tetrahedral background mesh of the entire computational domain is created that is agnostic to the particle shapes. This background mesh is read into Aria alongside the STL file that defines the geometry (either the spherical geometry or the reconstructed geometry). Elements of the background mesh that contain facets of the particle boundary are then automatically decomposed into smaller elements that conform to the interface described by the STL file. This procedure automatically generates multiple computational volumes that represent the electrolyte and each particle phase, and additionally creates the appropriate sidesets needed to apply the interfacial boundary conditions.

The mesh resulting from applying the CDFEM algorithm to Figure 4 is shown in Figure 5. Figure 5(a) shows a 3D representation of the mesh, and Figure 5(b) shows a 2D slice through a portion of the mesh. The new elements that sharply define the particle/electrolyte interface can be seen clearly. This approach is crucial for performing mesoscale simulations on a production scale, as it removes the burdensome, and oftentimes intractable, process of manually creating a computational mesh conforming to the particle and void phases. Also, it provides the sharp particle-electrolyte interface that the mechanical models require, rather than the volume-of-fluid or level-set based approaches that have previously been used.

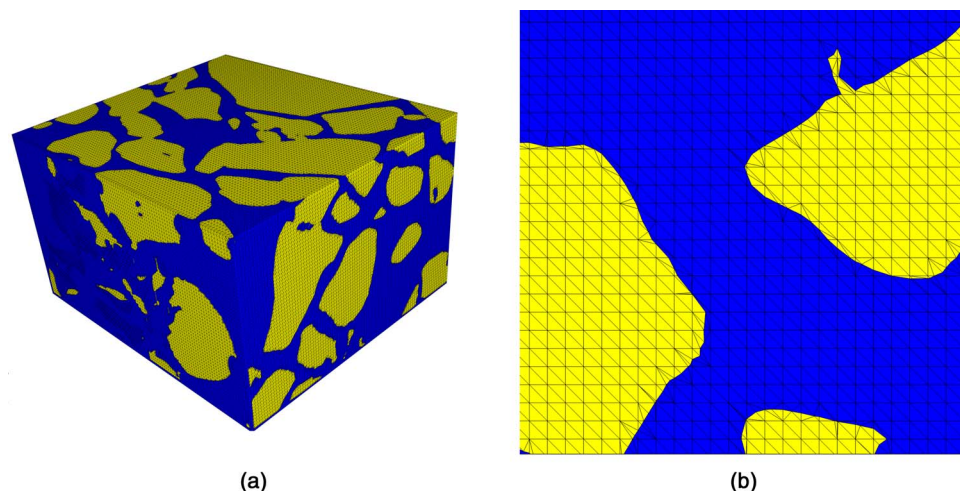


Figure 5. Background mesh decomposed with CDFEM using the 3D reconstruction and surface mesh of Figure 4. The particles are represented by the yellow elements, while the electrolyte, binder, and any void space is represented by the blue elements. (a) Three-dimensional visualization of the decomposed mesh. (b) Two-dimensional slice through the mesh, showing the details of the decomposition and interface representation.

Demonstration Problems

In this section, we demonstrate our numerical method on two example problems. First, we use the 3D reconstruction of the FIB/SEM data described in the “Reconstruction from experimental imaging” subsection to study the effect of swelling on an isotropic system. Second, anisotropic swelling is demonstrated on the NMC 111 spherical particle pack presented in subsection “Reconstruction from spherical particles”.

For both of these examples, the electrochemical model uses the parameter values $\kappa = 0.1 \text{ S/cm}$, $D_{\text{Li}^+} = 1.77 \times 10^{-6} \text{ cm}^2/\text{s}$, $D_{\text{PF}_6^-} = 4.88 \times 10^{-6} \text{ cm}^2/\text{s}$, $D_{\text{Li}} = 10^{-9} \text{ cm}^2/\text{s}$, and $j_0 = 2.6 \text{ mA/cm}^2$.²⁸ A 10C constant current discharge is modeled; such a high C-rate is chosen for demonstration purposes to ensure that noticeable gradients in C_{Li} are present within the particles. The elastic response of the particles is linear with Poisson’s ratio $\nu = 0.3$ and Young’s modulus $E = 10^{10} \text{ Pa}$.

For the mechanical model, no-penetration ($\mathbf{n} \cdot \mathbf{d} = 0$) conditions are applied to all external boundaries, with the implication that the electrode can’t macroscopically swell. However, the particles can slip along the external boundaries. While this may be appropriate in the x and y directions, where the computational volume is very small compared to the entire dimensions of the sample, it is unknown what

boundary conditions are most appropriate in the z direction, where the electrodes are thin. Future work will focus on identifying the effect of this boundary condition, along with considering additional boundary conditions, such as constant force or pressure. Boundary conditions for the electrochemical model are described in the “Model” section.

Isotropic swelling on experimental 3D reconstruction.— The three-dimensional reconstruction of the LiCoO_2 cathode is used to perform a coupled electrochemical-mechanical simulation. The domain is $20 \times 18 \times 12$ microns, which is the size of the reconstructed geometry, and the background mesh size is 0.5 micron, which leads to a relatively coarse simulation. For these simulations, the lithium-induced swelling is governed by $\beta_n = \beta_t = 10^3$.

The three-dimensional visualization shown in Figure 6 was taken at the end of this simulation, where the maximum stresses were observed. Figure 6(a) shows the intercalated lithium concentration in the particles. This shows that by the end of the simulation, the lithium concentration is relatively uniform throughout the particles, with only the largest particles having a lower concentration in the middle than the edges. Conversely, Figure 6(b) shows the (von Mises) stress distribution throughout the particles at the same point in time. The stress values vary wildly throughout the particle, with the highest concentrations seemingly localized near regions where two particles come

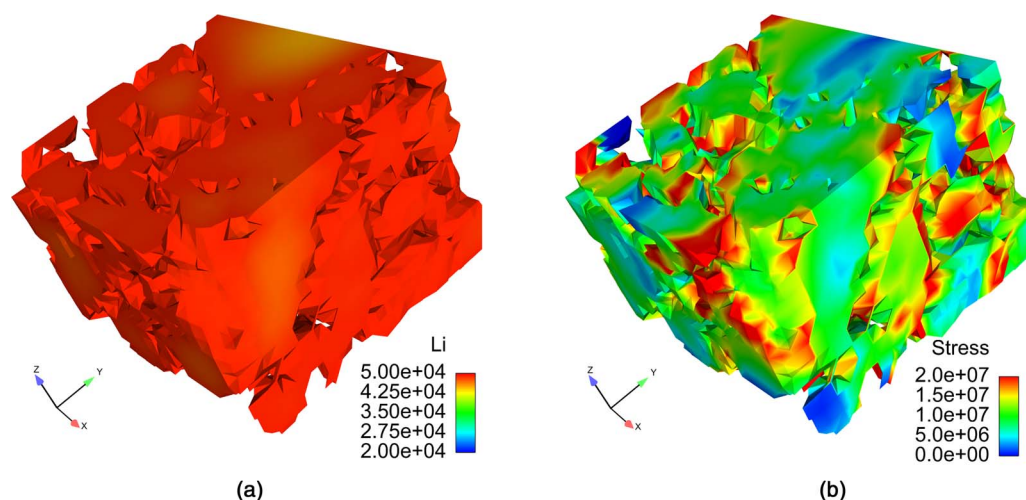


Figure 6. Three-dimensional snapshot at the end of the isotropic simulation, showing that high stress concentrations arise near particle contacts. (a) Lithium concentration in the solid electrolyte, in units of mol/m^3 . (b) Von Mises stress in the solid electrolyte, in units of Pascals.

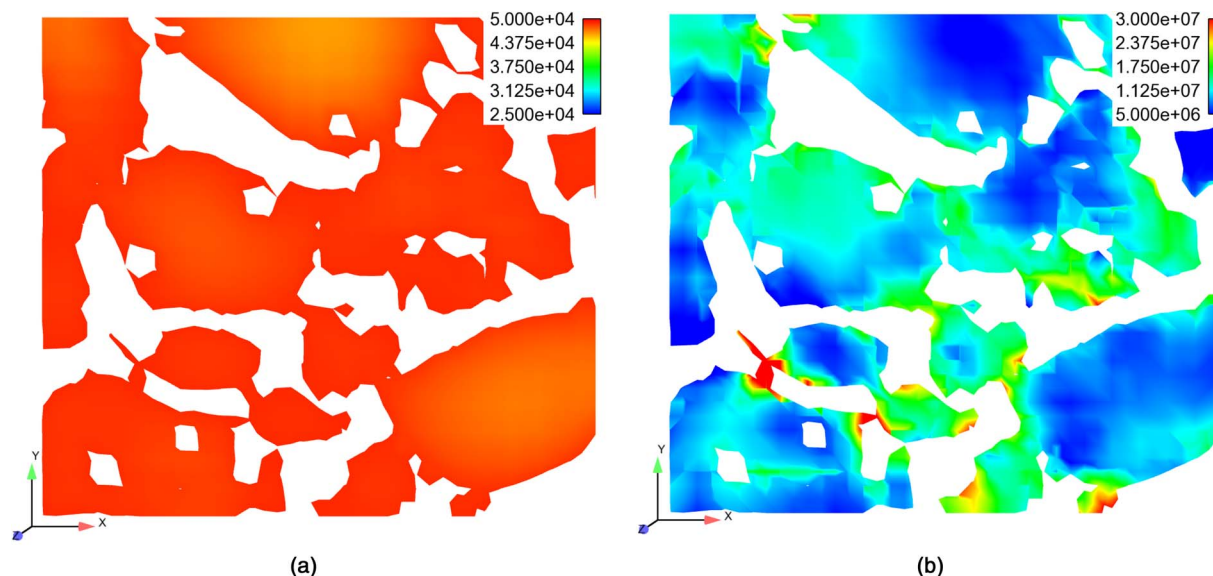


Figure 7. Two-dimensional slice in the z -plane for the isotropic simulation. (a) Lithium concentration in the solid electrolyte, in units of mol/m^3 . (b) Von Mises stress in the solid electrolyte, in units of Pascals.

into contact. Previous studies²⁶ show that the stress concentrations are the highest near small-scale surface features, a finding that is also shown in these simulations. However, our simulations suggest that the inter-particle confinement interactions cause larger stresses than small-feature-induced stresses in this system.

This behavior can be seen even more clearly in Figure 7, which shows a slice through the material perpendicular to the z -axis (electrode-to-electrode direction). The same quantities are shown in these two images as in Figure 6; the particle lithium concentration in Figure 7(a) and the von Mises stress in Figure 7(b). Figure 7(a) shows the same nearly-uniform lithium concentration profile. It is fairly clear from this lithium concentration, paired with the stress distribution in Figure 7(b), that concentration-gradient induced stresses are not the dominant mechanical player, illustrated by the larger particle at the top of the images that has a large lithium concentration gradient, but not a large stress. Higher stresses are seen near high-curvature features, such as in the center-bottom of Figure 7(b). However, the highest stresses appear at the particle-particle contacts shown in the lower-left of Figure 7(b), which supports the supposition that the constraints felt from nearby particles during the swelling process lead to the highest stresses. This type of behavior may be influenced by the choice of boundary conditions or the size of the domain, however, and these choices must be further investigated.

Unfortunately, however, it is difficult to tell from these images which high-curvature features are truly isolated from particle-particle contacts, and which are near these contacts. In the 2D visualizations of Figure 7, it is difficult to tell which features are in contact, but do not look that way because the true contact is slightly out of the visualization plane. Clearly, more simulations are needed to confirm the relative importance of these two phenomena, and we plan to develop a quantitative method to estimate this in future work. The ratios between the particle modulus, electrochemical charge/discharge rates, and the amount of swelling will all play a role in what the dominant set of physics are. Additionally, we have not considered the abrupt phase-change swelling used by Malave et al.,²⁶ which may lead to differences between their observations and ours. All of these considerations will be addressed in future work.

Anisotropic swelling on spherical particle pack.— In contrast to the previous section, where the lithiation strain was isotropic, in this section we use the anisotropic model described in the “Mechanics” subsection. For this example, the spherical particle reconstruction is

used to represent the particles. While this reconstruction is for a NMC 111 system, we continue to use LiCoO_2 electrochemistry for this demonstration. This particle pack is used because the spherical particles were originally created separately, allowing us to easily address each particle separately, which is required in order to assign each particle its own lattice orientation. The electrochemical parameters are the same as in the previous example, but in this example, the intercalation swelling anisotropy is exploited, with $\beta_t = \beta_n/10$. In this example, the crystal lattice orientation of each particle is assigned randomly, representing a random laydown of the particle pack. For this large of a difference between β_t and β_n , one would expect the displacement vectors in a single isolated particle to be oriented primarily in the lattice normal direction.

The effect of particle anisotropy can be clearly seen in Figure 8, which shows a 2D slice of a small extraction from this simulation rotated into 3D, with displacements show as 3D vectors. Here, we focus on the two large particles toward the top of the figure that are in contact. For isotropic, spherical particles that are isolated from other particles, one would expect a stress distribution that is spherically symmetric, along with displacements that are radially symmetric. For the large particle at the top-left of the figure, signs of this behavior can be seen toward the upper-left of the particle, where the stress seems to increase radially from the center out. However, due to the anisotropy of the material, the displacement vectors do not point outward radially, but instead are aligned with the crystal lattice normal direction, denoted by the purple coordinate system on the particle.

This behavior changes drastically near the $+x$ edge of the particle, where it makes contact with a second particle. The stress distribution and the displacement vector orientation changes significantly near this contact. Looking into the contacting particle (the larger particle at the upper-right of Figure 8), you can see a very high stress concentration near the contact, and the displacement vectors of the two particles are aligned. This alignment is in contrast to the displacements that would arise from the “natural” lattice orientation. This can be seen even more clearly with this second particle, where the natural orientation is in the $x - y$ plane, shown by the vectors at the lower-right of that particle. This change in the displacement orientations represents a shearing behavior that has not been previously reported. While some of these shear stresses may be due to the fact that our simulations do not allow slip between particles, it is unknown how important slip may be, as the friction between these packed particles, in the presence of compressive forces and electrolyte, is unknown.

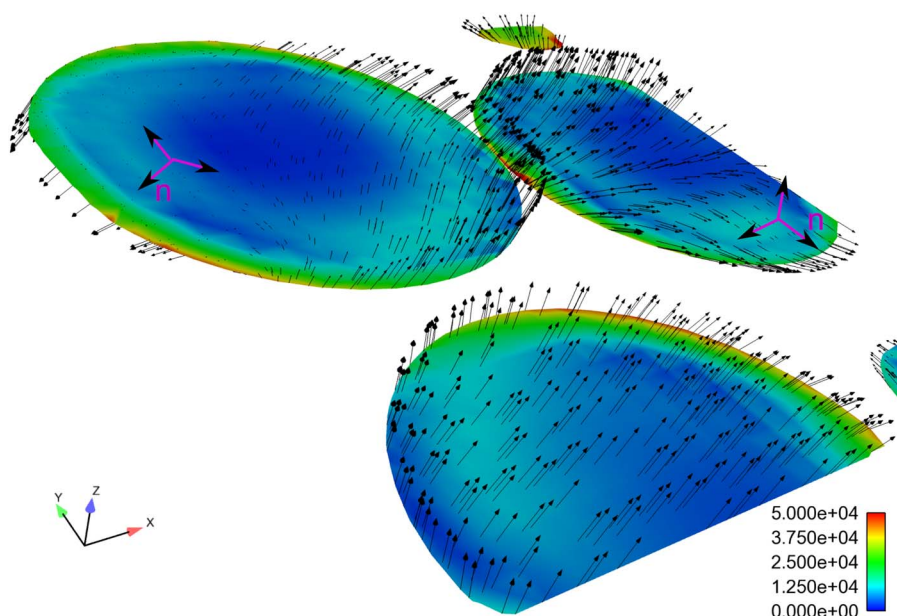


Figure 8. Two-dimensional slice in the z -plane for the anisotropic simulation, but oriented in three-dimensions. The slice is colored by the von Mises stress (in Pascals), and Lagrangian displacement vectors, a measure of particle deformation, are shown using black arrows. The local crystal lattice coordinate systems are shown with the purple arrows for two particles, with the normal direction indicated with an n .

Conclusions

In this paper, we presented a computational framework for modeling anisotropic, lithiation-induced mechanical deformation of cathode materials for lithium ion batteries. This model was presented in the context of the finite element method, and the simulations were conducted on the mesoscale, directly resolving many cathode particles and the surrounding electrolyte. Three-dimensional reconstructions of the cathode microstructure were created from both experimental FIB/SEM imaging¹⁷ and from spherical particle size distributions.³⁰ The computational mesh was created using novel CD-FEM techniques³⁹ directly from the three-dimensional reconstruction. This automatic mesh creation process greatly eases the burden of creating the computational mesh, which, if done manually, can be the most time-consuming part of these analyses. These simulations involved an electrochemical model based on a Butler-Volmer reaction rate²¹ coupled to a mechanical model involving a quasi-static linear elastic constitutive equation with anisotropic swelling strains that are linear in the local lithium concentration.

This work is unique from previous works in that it investigates the mechanics of the particle-to-particle contacts that arise in a real battery electrode microstructures, rather than looking at the mechanics of isolated particles. Using actual cathode microstructures, we demonstrated, for the first time, that for particles that swell isotropically, the largest stresses are located at the particle-to-particle contacts, due to neighboring particles constraining the swelling of a particle. While stress concentrations were also observed near small surface features, as discussed by Malave et al.,²⁶ the particle contact stresses were at least as large, if not larger, than the surface feature stresses, although we don't have large phase-change swelling.

Under anisotropic swelling conditions, we observed that isolated particles tend to swell (displace) along the direction normal to the lattice structure. However, when multiple particles are in contact, these particle-to-particle contacts lead to additional stresses and change the nature of the particle displacement. Near the contact region between two particles, the displacement vectors align, and the resulting direction may not be at all similar to the natural displacement of the more isolated regions of the particle. This effect gives rise to significant shear stresses in the particles that would not be present if the particles were isolated.

Clearly, further simulation work is required to learn more details about the relative importance of stresses generated from particle-to-particle contacts, those that arise from small features, and those that may arise from lithium concentration gradients. Which mechanism

dominates may depend on the nature of the microstructure itself (requiring reconstructions with a large number of particles or use of multiple reconstructions), the relative values of material properties, and the rate of charge/discharge. Capacity fade, as determined from the behavior of the electrochemical model, may only be elucidated by running simulations that span multiple charge-discharge cycles. We plan to perform these studies in future work and to use this simulation capability to study how the delithiation-induced swelling may lead to degradation of the percolated electrode structure, leading to capacity fade through many charge-discharge cycles.

Acknowledgments

The authors acknowledge Dan Bolinteanu for creating NMC 111 particle pack, including performing the drying simulations. Kyle Fenton measured the particle size distribution used for the NMC 111 particle pack. Scott Roberts appreciates many conversations with Dan Bolinteanu and Emilee Reinholz regarding three-dimensional reconstructions. Chris Apblett and Farid El Gabaly have provided much insight into battery performance and behaviors. We also appreciate Tobias Hutzenlaub for kindly providing the experimental images.

This work was funded as part of Sandia's Laboratory Directed Research and Development Program. Sandia National Laboratories is a multi-program laboratory managed and operated by Sandia Corporation, a wholly owned subsidiary of Lockheed Martin Corporation, for the U.S. Department of Energy's National Nuclear Security Administration under contract DE-AC04-94AL85000.

References

1. P. Arora, R. E. White, and M. Doyle, *J. Electrochem. Soc.*, **145**(10), 3647 (1998).
2. M. Kerlau, M. Marcinek, V. Srinivasan, and R. M. Kostecki, *Electrochimica Acta*, **52**(17), 5422 (2007).
3. J. H. Seo, M. Chung, M. Park, S. W. Han, X. Zhang, and A. M. Sastry, *J. Electrochem. Soc.*, **158**(4), A434 (2011).
4. J. Park, W. Lu, and A. M. Sastry, *J. Electrochem. Soc.*, **158**(2), A201 (2011).
5. M. Zhu, J. Park, and A. M. Sastry, *J. Electrochem. Soc.*, **159**(4), A492 (2012).
6. M. Ebner, F. Marone, M. Stamparoni, and V. Wood, *Science*, **342**(6159), 716 (2013).
7. J. N. Reimers and J. R. Dahn, *J. Electrochem. Soc.*, **139**(8), 2091 (1992).
8. G. G. Amatucci, J. M. Tarascon, and L. C. Klein, *J. Electrochem. Soc.*, **143**(3), 1114 (1996).
9. J. Cannarella and C. B. Arnold, *Journal of Power Sources*, **245**(0), 745 (2014).
10. P. R. Shearing, L. E. Howard, P. S. Jorgensen, N. P. Brandon, and S. J. Harris, *Electrochem. Commun.*, **12**, 374 (2010).
11. J. R. Wilson, J. S. Cronin, S. A. Barnett, and S. J. Harris, *Journal of Power Sources*, **196**(7), 3443 (2011).

12. J. Joos, T. Carraro, A. Weber, and E. Ivers-Tiffée, *J. Power Sources*, **196**, 7302 (2011).
13. S. J. Harris and P. Lu, *The Journal of Physical Chemistry C*, **117**(13), 6481 (2013).
14. Y. K. Chen-Wiegart, R. DeMike, C. Erdonmez, K. Thornton, S. A. Barnett, and J. Wang, *Journal of Power Sources*, **249**(0), 349 (2014).
15. S. Cooper, D. Eastwood, J. Gelb, G. Damblanc, D. Brett, R. Bradley, P. Withers, P. Lee, A. Marquis, N. Brandon, and P. Shearing, *Journal of Power Sources*, **247**(0), 1033 (2014).
16. M. Ender, J. Joos, and T. C. E. Ivers-Tiffée, *Electrochem. Commun.*, **13**, 166 (2011).
17. T. Hutzenlaub, S. Thiele, R. Zengerle, and C. Ziegler, *Electrochem. Solid-State Lett.*, **15**(3), A33 (2012).
18. G. B. Less, J. H. Seo, S. Han, A. M. Sastry, J. Zausch, A. Latz, S. Schmidt, C. Wieser, D. Kehrwald, and S. Fell, *J. Electrochem. Soc.*, **159**(6), A697 (2012).
19. A. H. Wiedemann, G. M. Goldin, S. A. Barnett, H. Zhu, and R. J. Kee, *Electrochimica Acta*, **88**(0), 580 (2013).
20. T. Hutzenlaub, S. Thiele, N. Paust, R. Spotnitz, R. Zengerle, and C. Walchshofer, *Electrochimica Acta*, **115**(0), 131 (2014).
21. M. D. Chung, J. H. Seo, X. C. Zhang, and A. M. Sastry, *J. Electrochem. Soc.*, **158**(4), A371 (2011).
22. N. Balke, E. A. Eliseev, S. Jesse, S. Kalnaus, C. Daniel, N. J. Dudney, A. N. Morozovska, and S. V. Kalinin, *J. Appl. Phys.*, **112**(5), 052020 (2012).
23. S. Yamakawa, H. Yamasaki, T. Koyama, and R. Asahi, *Journal of Power Sources*, **223**(0), 199 (2013).
24. A. Awarke, S. Lauer, M. Wittler, and S. Pischinger, *Computational Materials Science*, **50**(3), 871 (2011).
25. C. Lim, B. Yan, L. Yin, and L. Zhu, *Electrochimica Acta*, **75**(0), 279 (2012).
26. V. Malave, J. R. Berger, H. Zhu, and R. J. Kee, *Electrochimica Acta*, **130**(0), 707 (2014).
27. D.-W. Chung, P. R. Shearing, N. P. Brandon, S. J. Harris, and R. E. Garca, *J. Electrochem. Soc.*, **161**(3), A422 (2014).
28. M. Doyle and Y. Fuentes, *J. Electrochem. Soc.*, **150**(6), A706 (2003).
29. A. R. Denton and N. W. Ashcroft, *Phys. Rev. A*, **43**, 3161 (1991).
30. K. Fenton, *NMC 111 particle size distribution*. Personal Communication (2012).
31. S. Plimpton, *J. Comput. Phys.*, **117**(1), 1 (1995).
32. A. Kumar and J. J. L. Higdon, *Phys Rev E*, **82**(5), 051401 (2010).
33. A. Kumar, *Microscale dynamics in suspensions of non-spherical particles*. Ph.D. thesis, University of Illinois at Urbana-Champaign (2010).
34. L. E. Silbert, D. Ertaş, G. S. Grest, T. C. Halsey, D. Levine, and S. J. Plimpton, *Phys Rev E*, **64**(5), 051302 (2001).
35. P. A. Kralchevsky, V. N. Paunov, I. B. Ivanov, and K. Nagayama, *J Colloid Interf Sci*, **151**(1), 79 (1992).
36. T. Blacker, W. Bohnhoff, and T. Edwards, *CUBIT mesh generation environment. Volume 1: Users manual*. Technical report, SAND-94-1100, Sandia National Laboratories (1994).
37. M. A. Groeber and M. A. Jackson, *Integrating Materials and Manufacturing Innovation*, **3**(1), 5 (2014).
38. P. Notz, S. Subia, M. Hopkins, H. Moffat, and D. Noble, *Aria manual Aria 1.5: User's manual*. Technical Report SAND2007-2734, Sandia National Laboratories (2007).
39. D. R. Noble, E. P. Newren, and J. B. Lechman, *International Journal for Numerical Methods in Fluids*, **63**(6), 725 (2010).